RSC Advances

ROYAL SOCIETY OF CHEMISTRY

www.rsc.org/advances

The Preparation of Flowerlike $ZnMn_2O_4$ microspheres assembled with porous nanosheets and its lithium battery performance as anode materials

Xiangyun Zeng, Liuxue Shi, Linjie Li, Jiao Yang, Xi Cheng, Meizhen Gao*

Hierarchical flowerlike $ZnMn_2O_4$ microspheres with high electrochemical performance as an anode material for Li-Ion batteries have been fabricated by a facile solvothermal method.

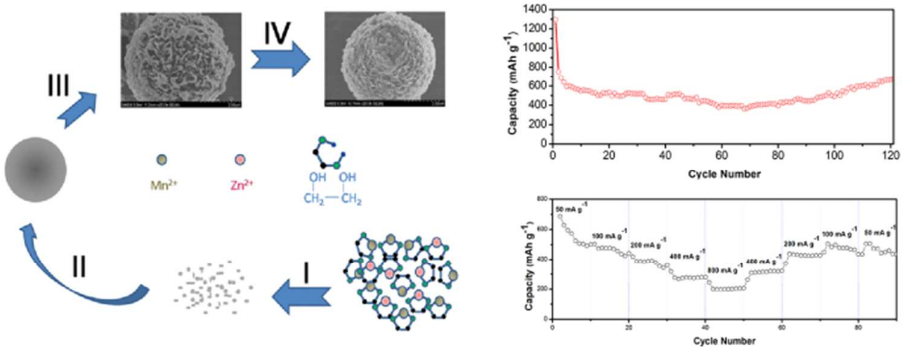

Abstract

In this paper, hierarchical $ZnMn_2O_4$ microspheres assembled with porous nanosheets have been synthesized by a facile solvothermal process and post annealing method. A possible formation mechanism for this unique structure is proposed based on a detailed time-dependent investigation. As a virtue of its beneficial structural features, the electrochemical tests of the as-synthesized hierarchical $ZnMn_2O_4$ microspheres exhibit an enhanced lithium storage capacity and an excellent cycling stability (662 mA h g^{-1} at 100 mA g^{-1} after 120 cycles). This may be attributed to their unique structural features of favoring the diffusion of Li^+ ions and electrode−electrolyte contacts during the electrochemical reaction and enhanced structural integrity with sufficient void space for buffering the volume variation during the Li^+ insertion and extraction. These results indicate that hierarchical $ZnMn_2O_4$ microspheres assembled with porous nanosheets are promising anode materials for highly reversible lithium-ion batteries.

1. Introduction

With the development of the society, one of the great challenges is undoubtedly energy storage. It is, therefore, essential to seek new materials to satisfy the increasing demands for energy conversion and storage.[1, 2] Over the past decades, various materials have been employed as anodes in Li-ion batteries (LIBs), such as carbon, Sn, Si, transition metal oxides and so on. Although non-carbonaceous materials Sn and Si anodes deliver higher capacities than carbon, unfortunately, their cycle life is poor because of materials disintegration due to the significant volume expansion during the charge and discharge cycling. Transition metal oxides (TMOs) have been widely investigated as high-capacity anodes for LIBs in view of their high theoretical capacities.[3-7] In particular, Fe_2O_3, MnO_2, V_2O_5, NiO_2 and Co_3O_4 have been among the widely investigated alternative anode materials for use in LIBs over the past decades. Among them, Co_3O_4 has shown the best anodic performance. [8, 9] However, due to the fact that Co_3O_4 is high cost, toxicity, and high lithium redox potential (2.2-2.4 V vs. Li^+/Li), [10] serious efforts are made toward replacing Co_3O_4 by eco-friendly and cheaper alternative metals. To this end, preliminary anodic properties have been reported on MCo_2O_4(M = Ni, Cu, Zn, etc.)[11-18] and NMn_2O_4 (N = Li, Ni, Zn, Co, etc.),[10, 19-26] which are isostructural to the spinel Co_3O_4.

Among various binary metal oxides above, Mn based anodes are considered as very promising electrode materials, because manganese is more environmentally benign, much cheaper and more abundant in nature compared to cobalt. Apparently, these prominent features make Mn based binary metal oxides ideal materials to replace Co_3O_4 as electrode materials. $ZnMn_2O_4$ is selected as the research material because of its excellent chemical and physical properties, such as its high theoretical capacity of 784 mA h g^{-1}.[10] Recently, some research results on $ZnMn_2O_4$ with different nanostructures as high-capacity anodes for lithium-ion batteries have been reported. For example, Zhang et al. have synthesized $ZnMn_2O_4$ superstructures with capacity values as high as 626 mA h g^{-1} after 50 discharge–charge cycles at a current rate of 100 mA g^{-1}.[27] Low and co-workers have described a facile method to prepare $ZnMn_2O_4$ hollow microspheres exhibiting a high discharge capacity of 607 mA h g^{-1} after 100 discharge–charge cycles at 400 mA g^{-1}.[10] Recent reports showed that orientated self-assembled/self-supported microsphere structures can help to enhance electrochemical performance because they can enhance the electrochemical kinetics, shorten the diffusion distance for lithium ions and accommodate the volume change during the lithium intercalation and de-intercalation processes.[13, 28-32]

Herein, we present a facile solvothermal method to directly synthesis the hierarchical flowerlike $ZnMn_2O_4$ precursor microspheres, which assembled with nanosheets. The formation mechanism of the flowerlike hierarchical microspheres structure has been studied. After an annealing treatment at high temperature under 600□ in air, highly crystalline hierarchical $ZnMn_2O_4$ microspheres assembled with porous nanosheets can be obtained. In addition, we demonstrate that such hierarchically structured spinel $ZnMn_2O_4$ porous nanosheets-based microspheres exhibit superior rate capability and cycling stability as cathode materials for LIBs.

2. Experimental

Synthesis

In this work, all reagents are analytical grade and are used as raw materials without further purification. In a typical synthesis of $ZnMn_2O_4$ hierarchical microspheres, 2.5 g polyethylene glycol 800 is firstly dissolved in 75 ml ethylene glycol to form a transparent solution. Then, 1.25 mmol $Zn(CH_3COO)_2 \cdot 4H_2O$ and 2.5 mmol $Mn(CH_3COO)_2 \cdot 4H_2O$ are added into the clear solution. After being stirred vigorously for 4 h, the obtained solution is transferred into a 100 ml Teflon-lined stainless steel autoclave. After 12 h hydrothermal treatment at 200 □， the taupe ZnMn-glycolate is obtained by filtering and washing several times with ethanol and dried at 80 □ under oven. After calcined for 5 h in air, the $ZnMn_2O_4$ hierarchical microspheres are obtained. The temperature and heating rate are 600 □ and 2 □/min respectively.

Characterization

The crystal phase, morphology and composition of the products are characterized by X-ray powder diffraction (XRD, Rigaku, RINT2400) with Cu Kα radiation (λ = 1.5418 Å), field-emission scanning electron microscopy (FE-SEM, Hitachi, S-4800), energy dispersive spectrometer (EDS, Thermo, Noran System Six 300) and transmission electron microscope (TEM, FEI, Tecnai G2 F30). Surface analysis of the samples is performed using XPS (XPS, Kratos, AXIS Ultra). FTIR spectrum of the precursor is recorded between 400 and 4000 cm^{-1} on a Nicolet NEXUS 670 FTIR spectrometer. Thermogravimetric analysis (TGA) is carried out in air at a heating rate of 1.00 °C/min from 35.00 □ to 700.00 □ using a Perkin Elmer Diamond TG/DTA instrument. The measurements of the specific surface area and the analysis of the porosity of hierarchical $ZnMn_2O_4$ microspheres are performed through N_2 adsorption−desorption isotherms at 77 K, using a Micrometrics ASAP 2020 M system.

Electrochemical Measurements

The electrochemical properties of anode materials of lithium-ion battery are evaluated by using two-electrode coin cells (size: 2032) with lithium serving as both the counter electrode and the reference electrode. Each working electrode was prepared by mixing 80 wt % active material (e.g., as-prepared hierarchical $ZnMn_2O_4$ microspheres), 10 wt % conducting agent (AB, acetylene black) and 10 wt % binder (polyvinylidene difluoride, PVDF) with aid of N-methyl-2-pyrrolidone (NMP) to form a homogeneous slurry, which is then coated onto a copper foil. The electrodes are dried at 110 □ in a vacuum oven for 10 h before assembling. After being pressed, the electrodes are assembled into coin cells (CR2032) in an argon-filled glove box by using 1 mol/L LiPF6 in ethylenecarbonate (EC) and diethylenecarbonate (DEC) (1:1, v/v) as the electrolyte. Galvanostatic charge/discharge is conducted using a CT2001A cell test instrument (LAND Electronic Co.) with a voltage window of 0.01−3.0 V at a setting current rate.

3. Results and discussion

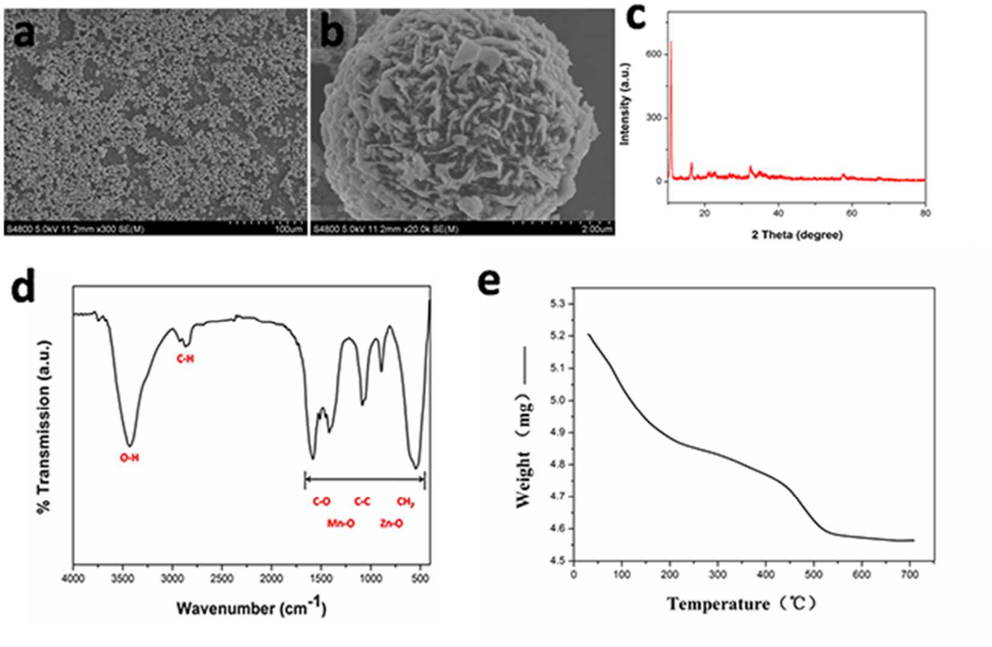

Figure 1 (a, b) SEM images of the precursor of flowerlike $ZnMn_2O_4$ microspheres, (c) XRD pattern, (d) FTIR spectrum and (e) TGA of the precursor of flowerlike $ZnMn_2O_4$ microspheres.

The morphology of the as-prepared precursor obtained after solvothermal treatment is observed by the FESEM. As shown in the panoramic image (Figure 1a), these microspheres of the precursor are uniform with an average size of about 5 μm and without serious aggregation. A magnified FESEM image reveals that the surface of the microsphere is composed of fine nanosheets which possess a thickness of about 70 nm (Figure 1b). It’s easy to discern that the conductivity of the precursor is poor from the FESEM image. This phenomenon is due to metal hydroxide could be formed and crystallized together with organic ligands in an alkaline environment under the solvothermal conditions. In order to verify this, the structure of the as-prepared hierarchical microspheres is examined by XRD and the molecular structure and functional groups are characterized by FTIR spectrum. As shown in Figure 1c, the crystalline of the precursor, which is similar to the XRD patterns of Mn-EG, Zn-Mn-EG and Zn-EG.[33-35] Figure 1d shows the FTIR spectrum of the precursor. The strong absorption bands lying in 2500-3000 cm^{-1} are characteristic of the C–H stretching mode. With the exception of this δH_2O vibration, all the bands located below 2000 cm^{-1} are due to Mn-O, Zn-O, C-C, C-O and CH_2 bond.[33, 34] The strong signal at 3400 cm^{-1} clues for loosely bonded OH groups. According to the TG curve as showed in Figure 1e, a temperature of 600 ℃ is chosen for thermal treatment of the precursor to ensure its complete decomposition.

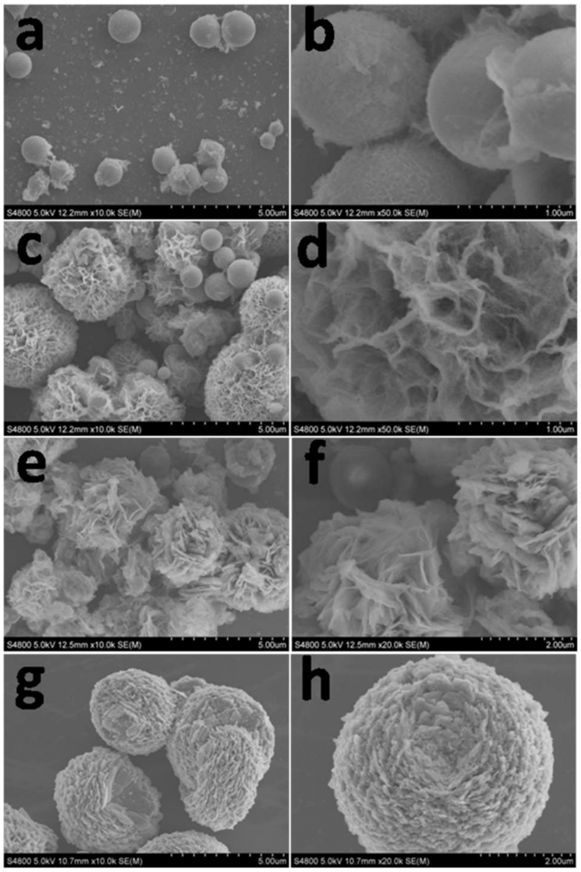

Figure 2 SEM images of the precursor of flowerlike $ZnMn_2O_4$ microspheres prepared with differentreaction durations. a, b) 1.5 h; c, d) 3 h; e, f) 6 h; g, h) 12 h.

In order to obtain a better understanding of the formation mechanism of the flower-like $ZnMn_2O_4$ hierarchical superstructures, the products formed at different growth stages are collected and examined by SEM. The morphologies are shown in Figure 2. In the initial stage, the precursors are microspheres composed with nanoparticles and some small nanosheets on the surface (Figure 2a and b). After 3 h of hydrothermal treatment, both microspheres and the hierarchical structures can be found, but the nanosheets are loose and irregular (Figure 2c and d). After 6 h, the superstructures then gradually ripe, however there are still a few spheres as shown in Figure 2e and f, and the compact density of the nanosheets is not high. Finally, the perfect flower-like $ZnMn_2O_4$ hierarchical microspheres assembled with highly compact porous nanosheets are obtained after 12 h (Figure 2g and h).

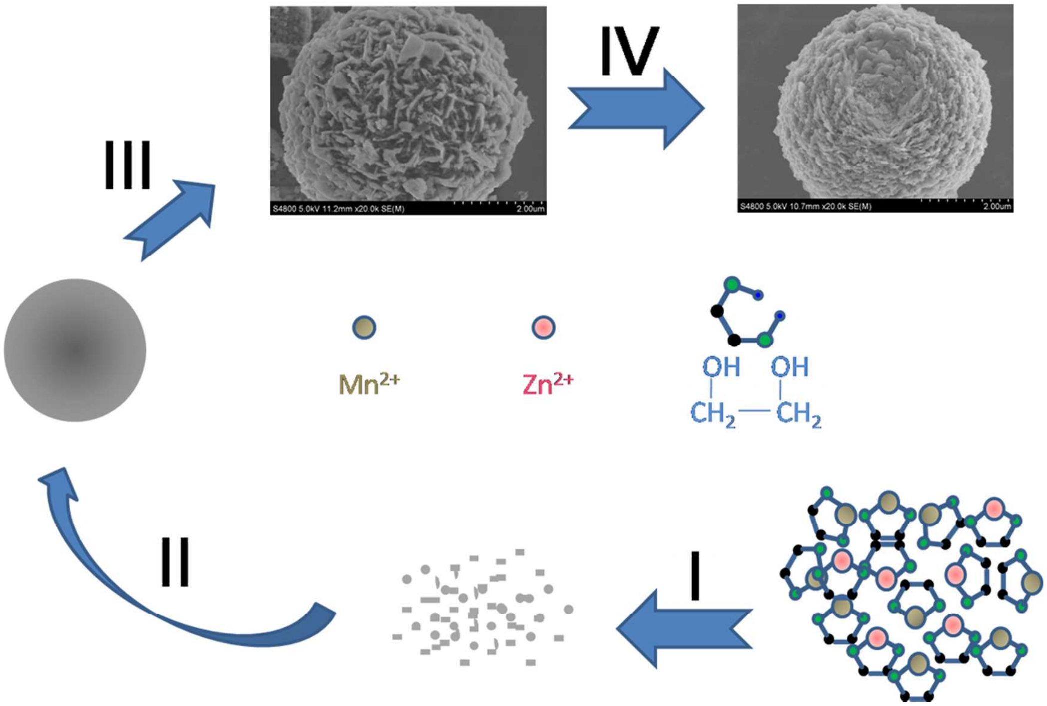

Figure 3 Illustration of the formation of $ZnMn_2O_4$ hollow flowers through the Ostwald ripening process.

Based on the time-dependent experiment results, the formation mechanism of the flower-like $ZnMn_2O_4$ hierarchical microspheres is proposed to proceed via a four-step process as depicted in Figure 3. The first step consists of precipitation of metal alkoxide particles from ethanediol solutions of salts. A number of nuclei generate during the initial period and subsequently form primary particles by diffusion of metal glycolates or alkoxide molecularly to the nuclei. (Step I) During the solvothermal process, the main metal glycolates or alkoxide molecular resulting from acid-base equilibrium reactions are believed to form as follows:[36, 37]

$$HOCH_2CH_2OH \leftrightarrow CH_3CHO + H_2O \quad (1)$$

$$CH_3COO + H_2O \leftrightarrow CH_3COOH + OH^- \quad (2)$$

$$HOCH_2CH_2OH + 2OH^- \leftrightarrow (CH_2)_2(O^-)_2 + H_2O \quad (3)$$

$$(CH_2)_2(O^-)_2 + Zn^{2+} \leftrightarrow (CH_2)_2(O)_2Zn \quad (4)$$

$$(CH_2)_2(O^-)_2 + Mn^{2+} \leftrightarrow (CH_2)_2(O)_2Mn \quad (5)$$

In the following stage, these primary particles quickly aggregate into nanospheres driven by the minimization of surface free energy with a size on the micrometer scale, which serve as the cores of the flower-like structures. This particular aggregation process of the particle formation of various monodispersed oxides has been reported by Ocana et al.[38] and the formation of microspheres seems to follow the scheme proposed by LaMer et al..[39] Moreover, the surfactant molecules providing coordination sites for cations can cap on the surface of the nanospheres, which may be helpful for avoiding the over growth of the nanospheres, resulting in uniformly discrete products, and the EG can act not only as a solvent in the process, but also as a stabilizer to prevent the particles from agglomerating.[31, 40] (Step Ⅱ) Meanwhile, the concentration of the reactants in the surrounding solution decreases, which bring about the fall of the supersaturation and a chemical equilibrium is established between the solid-liquid interface. As the hydrothermal reaction proceeds, some interior crystallites are still in nonequilibrium state. In this process, the exterior crystallites will serve as starting points to attract the interior metastable crystallites underneath the surface layer. [41] In order to recover the solution from the nonequilibrium state, many of the nanocrystallites in the solution transfer onto the nanospheres, which results in secondary deposition on the exterior surface.[12] Owing to highly intrinsic platelike growth habit of zinc oxides and manganese oxides and a simple array of the nanoplates will easily generate a curvature, the new deposition process results in surface nanoflakes.[23, 42] (Step Ⅲ) At the last stage, some nanoplates continue to grow larger by combining with remaining particles in the solution with increasing aging time, the inner core is consumed through this dissolution-recrystallization process, possibly because of Ostwald ripening according to the well-known Gibbs–Thomson law.[43] The beautiful flower-like $ZnMn_2O_4$ hierarchical microspheres consisting of nanosheets are obtained when the inner core is completely consumed. (Step Ⅳ)

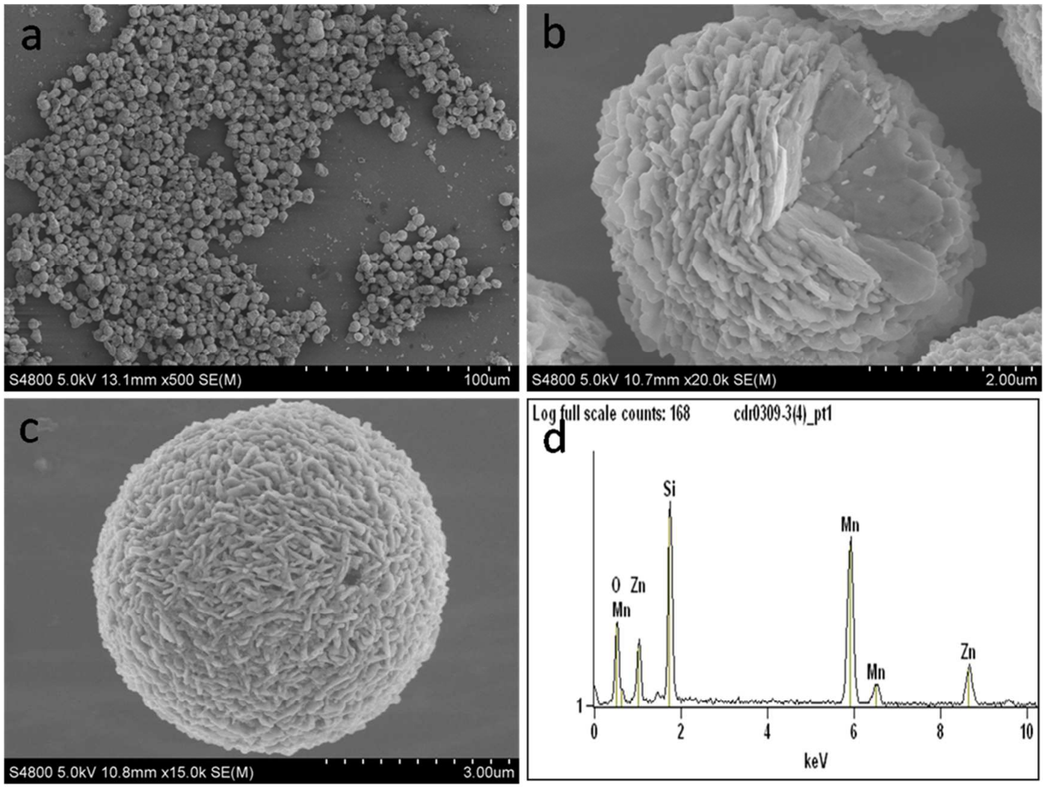

Figure 4 (a, b, c) SEM images and (d) EDS spectrum of the flowerlike $ZnMn_2O_4$ microspheres.

Figure 4 shows the general and high-magnification SEM images of the final product, which obtained after treating the as-prepared precursor at 600 ℃ for 5 h in air. The low-magnification SEM image (Figure 4a) reveals that the as-made $ZnMn_2O_4$ products are uniform and monodisperse microspheres with diameters of 4–6 μm without structural collapse. Compared with the as-prepared precursor (Figure 1a), after thermal decomposition at 600 ℃ for 5 h, the $ZnMn_2O_4$ products still maintain the structure and morphology integrity and the hierarchical microstructures are quite thermally stable. The high-magnification SEM images (Figure 4b, c) further indicate that these microspheres assembled with nanosheets, which have the thickness of 50-80 nm. The EDS spectrum (Figure 4d) reveals that these nanostructures are mainly composed of the elements Zn, Mn and O and the Mn/Zn ratio perfectly agrees with that in $ZnMn_2O_4$, indicating that pure flowerlike $ZnMn_2O_4$ microspheres are obtained. The silicon peak is considered to be caused by the silicon substrate.

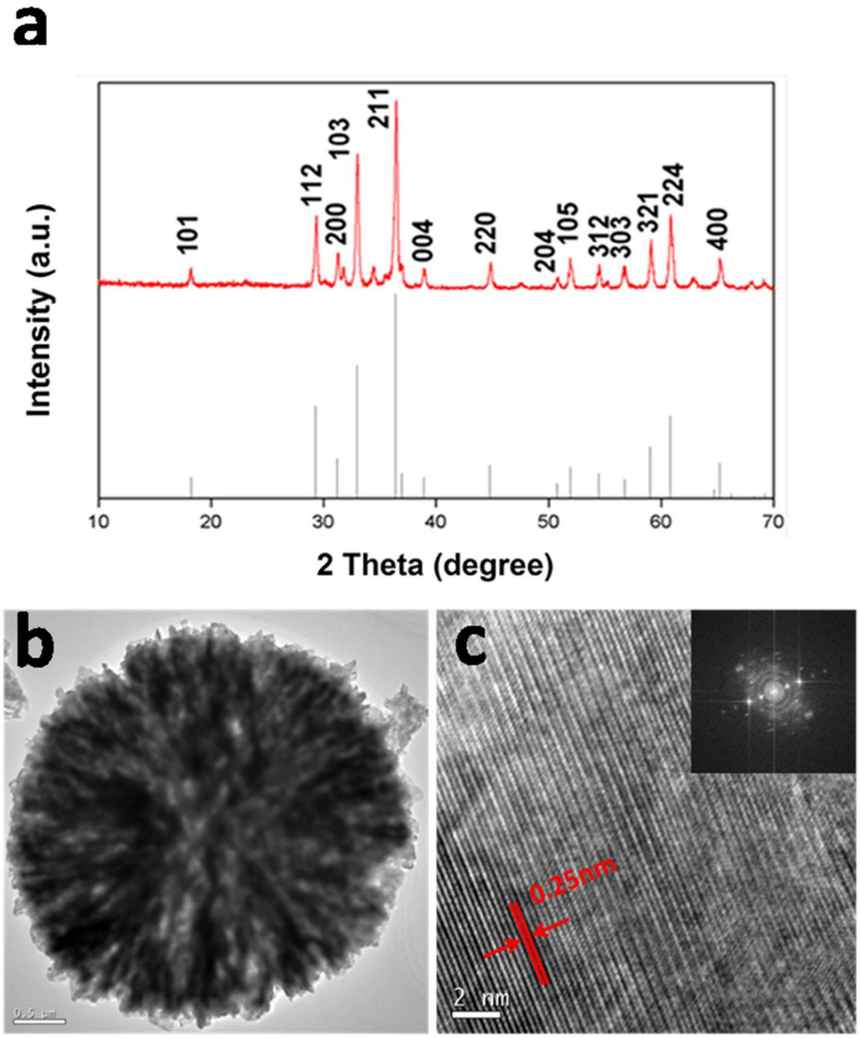

Figure 5 (a) XRD pattern and (b, c) TEM and HRTEM images of the flowerlike $ZnMn_2O_4$ microspheres.

The XRD pattern of the product is shown in Figure 5a. All of the diffraction peaks in this pattern could be assigned to tetragonal $ZnMn_2O_4$ structure, which are in a good agreement with the standard values (JCPDS: 24-1133). No peaks of impurities can be detected from this pattern. The detailed structure of hierarchical $ZnMn_2O_4$ microspheres is further characterized by transmission electron microscope (TEM) as shown in Figure 5b. In agreement with the above described FESEM observation, the TEM image of a single hierarchical $ZnMn_2O_4$ microspheres clearly demonstrate that the microspheres assembled with porous nanosheets, which have the thicknesses of 50-80 nm. Figure 5c shows the HRTEM image of microspheres, from which the interlayer distance of randomly selected nanosheet is calculated to be 0.25 nm, which corresponds well to the lattice spacing of the (211) plane of tetragonal $ZnMn_2O_4$.

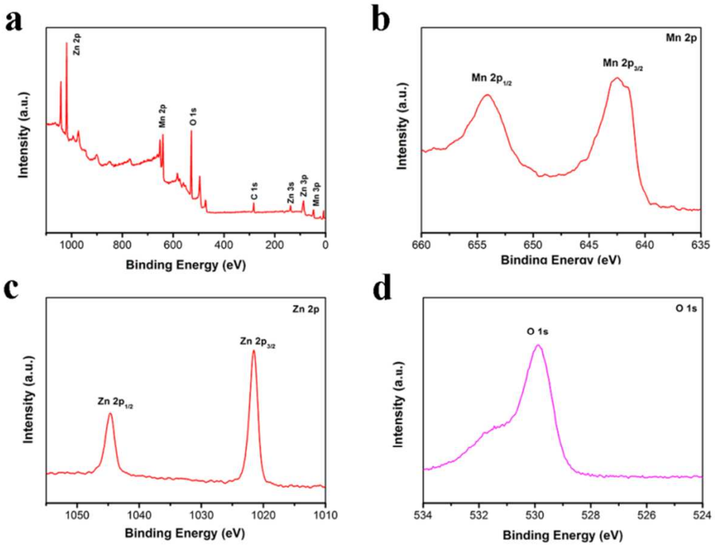

Figure 6 XPS spectra of the $ZnMn_2O_4$ samples: (a) survey spectrum; (b) Mn 2p spectrum; (c) Zn 2p spectrum; (d) O 1s spectrum.

XPS was used to further confirm the formation of $ZnMn_2O_4$. As shown in Figure 6a, the signals of Zn, Mn and O as well as C can be identified. The presence of carbon at 284.8 eV in the spectrum can be assigned to carbon contamination. The Mn 2p spectrum displays a $2p_{3/2}$ and $2p_{1/2}$ spin-orbit doublet at 642.5 and 653.9 eV as presented in Figure 6b. The separation of the two signals is 11.4 eV, which is consistent with the Mn^{III} in $ZnMn_2O_4$ materials reported previously,[44] and strongly confirms the fact that the Mn^{IV} has been completely reduced. Figure 6c shows the Zn 2p peaks at binding energies of 1021.6 and 1044.5 eV, which can be attributed to the Zn $2p_{1/2}$ and Zn $2p_{3/2}$ respectively. Additionally, the energy difference between the Zn $2p_{1/2}$ and Zn $2p_{3/2}$ peaks is 22.9 eV, which is in line with previous reports.[45] Meanwhile, O 1s spectra of $ZnMn_2O_4$ can be found at 529.9 eV, which is a characteristic of oxygen in metal oxides.(Figure 6d)[46]

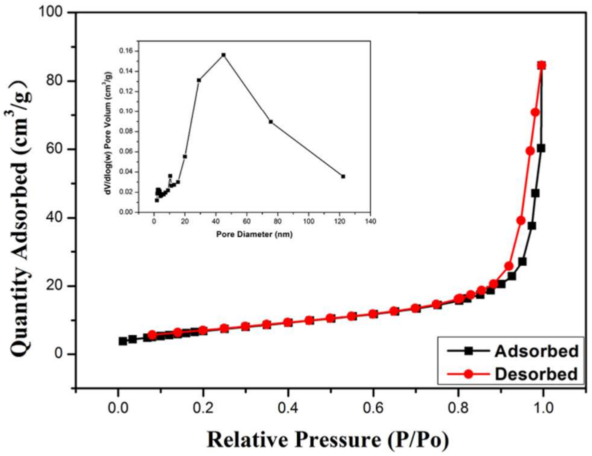

Figure 7 Nitrogen adsorption−desorption isotherm of the $ZnMn_2O_4$ microspheres, the inset shows the pore size distribution.

Figure 7 shows the nitrogen adsorption-desorption isotherms and the corresponding Barret-Joyner-Halenda (BJH) pore size distribution curves of the obtained flower-like $ZnMn_2O_4$ microspheres. The adsorption isotherm for flower-like $ZnMn_2O_4$ microspheres is a typical IV curve, indicating mesoporous characteristic. The measured

Brunauer-Emmett-Teller (BET) area is 26.1 m^2g^{-1}, and the average pore diameter of $ZnMn_2O_4$ is about 20.1 nm, which is calculated from the desorption branch of the nitrogen isotherm with the BJH method. The corresponding BJH desorption cumulative pore volume is about 0.1309 cm^3g^{-1}. In consideration of the mesoporous structure of $ZnMn_2O_4$ microspheres, it's expected to improve the electrochemical performance by favoring the diffusion of Li^+ ions and electrode−electrolyte contacts during the electrochemical reaction.

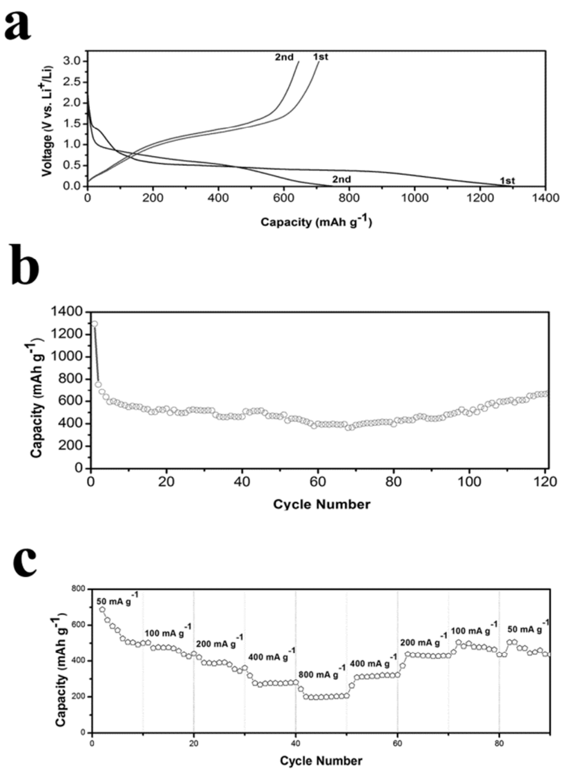

Figure 8 (a) Charge and discharge voltage profiles for the first and second cycles at a current density of 100 mA g^{-1}; (b) Cycling performance at a current density of 100 mA g^{-1}. (c) Rate capability test at various current densities of the electrode made from flowerlike $ZnMn_2O_4$ microspheres.

In order to examine the potential application of the flowerlike $ZnMn_2O_4$ microspheres as anode for lithium-ion batteries, lithium storage properties of the obtained materials are tested using the standard $ZnMn_2O_4$/Li half-cell configuration at room temperature (RT = 25 °C). Figure 8a shows typical charge-discharge curves for the first and second cycles of the $ZnMn_2O_4$ electrode at a current density of 100 mA g^{-1} in the potential range between 0.01 and 3.00 V. During the first discharge, the voltage decreased steeply to approximately 1.4 V, whereupon a small plateau sets with 0.15 mol of lithium ion intercalation reaction, a large and steady plateau at 0.5 V with overall capacity of ~870 mA h g^{-1} (corresponds to ~7.8 mol of Li per mol of $ZnMn_2O_4$) follows by a slope till 0.005 V and a capacity of ~359 mA h g^{-1} (~3.8 mol of Li). The overall first discharge capacity 1259 mA h g^{-1} corresponds to ~11.6 mol of Li, which is higher than the theoretical value (1008 mA h g^{-1}) based on the reaction: $ZnMn_2O_4 + 9Li + 9e^- \rightarrow ZnLi + 2Mn + 4Li_2O$. The extra Li consumption could be attributed to the decomposition of the electrolyte at low voltages generating a solid electrolyte interphase (SEI) layer and a polymeric gel-type layer at the $ZnMn_2O_4$/electrolyte interface. The first charge curve from 0.01 to 3.00 V shows a steady and smooth voltage increase with an overall specific capacity of 707 mA h g^{-1}, indicating a different electrochemical mechanism from the first discharge. Thus, there is an irreversible specific capacity loss between the first discharge and charge cycles. The large irreversible capacity loss of the first cycle might be caused by the phenomenon that the formed SEI film could not decompose completely during the first charge. The voltage–capacity profile of $ZnMn_2O_4$ for the second discharge reaction is at variance with the first-discharge reaction (Figure 7a). The potential plateau shifts upward to nearly 0.60 V (versus Li^+/Li) with a more sloping profile accompanied by the disappearance of the small plateau at about 1.40 V. Nevertheless, the overall discharge capacity of 750 mA h g^{-1} in the second discharge process is retained. The initial charge capacity and the second discharge capacity are 707 and 750 mA h g, that match well with the theoretical value (784 mA h g^{-1}) based on the reaction: $ZnLi + 2Mn + 3Li_2O \leftrightarrow ZnO + 2MnO + 7Li^+ + 7e^-$.

Figure 8b shows the discharge and charge capacity versus cycle numbers up to 120 cycles. As can be seen, the charge capacity decreases gradually to 388 mA h g^{-1} for the first 70 cycles. Interestingly, the capacity then starts to increase and a high discharge capacity of 662 mA h g^{-1} is retained after 120 discharge–charge cycles, corresponding to 88% of the second discharge capacity, demonstrating the high reversible specific capacity and long cycle life of the anode. It is interesting to note the phenomenon of the gradual increased capacity, which is well-documented in the literature, and is attributed to the reversible growth of a polymeric gel-like film resulting from kinetically activated electrolyte degradation.[35, 47, 48] To better understand the electrochemical behavior of the flowerlike $ZnMn_2O_4$ microspheres, the rate performance at various current densities (50–800 mA g^{-1}) in the voltage range of 0.01–3.0 V is also investigated and shown in Figure 8c. The cell shows good rate capability with average discharge capacity of 557, 460, 375, 276, and 201 mA h g^{-1}, when the current density increases stepwise to 50, 100, 200, 400, 800 mA g^{-1}, respectively. After high-rate charge-discharge cycling, the current density is reduced stepwise to 50 mA g^{-1}, with a specific capacity as high as 477 mA h g^{-1} recovered. The improved electrochemical performance of $ZnMn_2O_4$ might be partly attributed to its unique structure of assemblies of nanoplates. On one hand, the micro-sized hierarchical structure composed of nano-sized nanoplates with pores effectively increases the electrode−electrolyte contact area for more Li^+ migration across the interface, shortens the Li^+ ion and electrons diffusion length, and accommodates the structural strain and volume change during the charge and discharge cycle, thus leads to high specific capacity and superior rate capability. On the other hand, the open space between neighboring nanoplates allows for easy diffusion of the electrolyte, ensuring every nanoplate can take part in the electrochemical reaction because each nanoplate is in contact with electrolyte.

4. Conclusion

In summary, we successfully synthesized hierarchical $ZnMn_2O_4$ microspheres assembled with porous nanosheets by a facile solvothermal process and post annealing treatment. A possible formation mechanism for this unique structure is proposed based on a detailed time-dependent investigation. Benefitting from its structural features, the electrochemical tests of as-synthesized hierarchical $ZnMn_2O_4$ microspheres exhibits an enhanced lithium storage capacity and an excellent cycling stability (662 mA h g^{-1} at 100 mA g^{-1} after 120 cycles). The enhanced electrochemical performance may be attributed to their unique structural features of favoring the diffusion of Li^+ ions and electrode−electrolyte contacts during the electrochemical reaction and enhanced structural integrity with sufficient void space for buffering the volume variation during the Li^+ insertion/extraction. In consideration of its electrochemical performance and simple preparation process, the hierarchical $ZnMn_2O_4$ microspheres might serve as a potential candidate for high-capacity anode material in LIBs. This facile strategy may be extended to synthesize other manganite microspheres assembled with porous nanosheets, which are very promising in energy storage and conversion because of their unique structural features.

Acknowledgements

This work was financially supported by the NSFC (No. 51371093) and the MOE (No. IRT1251 & 20130211130003) of China.

Notes

[a] *Key Laboratory for Magnetism and Magnetic Materials of Ministry of Education, Lanzhou University, 730000 Lanzhou,*

People's Republic of China

[b] *School of Physical Science and Technology, Lanzhou University, Lanzhou, Gansu 730000, People's Republic of China. E-mail: zengxy08@163.com; gaomz@lzu.edu.cn; Tel: +86 931 8914160*

References

1. J.-M. Tarascon and M. Armand, Nature, 2001, **414**, 359-367.
2. M. Armand and J.-M. Tarascon, Nature, 2008, **451**, 652-657.
3. P. Poizot, S. Laruelle, S. Grugeon, L. Dupont and J. Tarascon, Nature, 2000, **407**, 496-499.
4. X. Z. Yu, B. A. Lu and Z Xu, Advanced Materials, 2014, **26**, 1044-1051.
5. C. Z. Yuan, L. H. Zhang, S. Q. Zhu, H. Cao, J. D. Lin and L. R. Hou, Nanotechnology, 2015, **26**, 145401.
6. J. Zhu, Z. Xu and B. A. Lu, Nano Energy, 2014, **7**, 114-123.
7. W. J. Jiang, W. Y. Zeng, Z. S. Ma, Y. Pan, J. G. Lin and C. S. Lu, RSC Advances, 2014, 4, 41281-41286.
8. J. Wang, N. Yang, H. Tang, Z. Dong, Q. Jin, M. Yang, D. Kisailus, H. Zhao, Z. Tang and D. Wang, Angewandte Chemie, 2013, **125**, 6545-6548.
9. X. Wang, X. L. Wu, Y. G. Guo, Y. Zhong, X. Cao, Y. Ma and J. Yao, Advanced Functional Materials, 2010, **20**, 1680-1686.
10. L. Zhou, H. B. Wu, T. Zhu and X. W. D. Lou, Journal of Materials Chemistry, 2012, **22**, 827-829.
11. Y. Sharma, N. Sharma, G. Rao and B. Chowdari, Journal of Power Sources, 2007, **173**, 495-501.
12. L. Li, Y. Cheah, Y. Ko, P. Teh, G. Wee, C. Wong, S. Peng and M. Srinivasan, Journal of Materials Chemistry A, 2013, **1**, 10935-10941.
13. J. Li, S. Xiong, Y. Liu, Z. Ju and Y. Qian, ACS Applied Materials & Interfaces, 2013, **5**, 981-988.
14. N. Du, Y. Xu, H. Zhang, J. Yu, C. Zhai and D. Yang, Inorganic Chemistry, 2011, **50**, 3320-3324.
15. Y. Sharma, N. Sharma, G. Subba Rao and B. Chowdari, Advanced Functional Materials, 2007, **17**, 2855-2861.
16. G. Zhang and X. W. D. Lou, Scientific Reports, 2013, **3**, 1470.
17. J. Liu, C. Liu, Y. Wan, W. Liu, Z. Ma, S. Ji, J. Wang, Y. Zhou, P. Hodgson and Y. Li, CrystEngComm, 2013, **15**, 1578-1585.
18. W. Kang, Y. Tang, W. Li, Z. Li, X. Yang, J. Xu and C.-S. Lee, Nanoscale, 2014, **6**, 6551-6556.
19. E. Hosono, T. Kudo, I. Honma, H. Matsuda and H. Zhou, Nano letters, 2009, **9**, 1045-1051.
20. D. K. Kim, P. Muralidharan, H.-W. Lee, R. Ruffo, Y. Yang, C. K. Chan, H. Peng, R. A. Huggins and Y. Cui, Nano letters, 2008, **8**, 3948-3952.
21. L. Zhou, D. Zhao and X. W. Lou, Advanced Materials, 2012, **24**, 745-748.
22. L. Wang, B. Liu, S. Ran, L. Wang, L. Gao, F. Qu, D. Chen and G. Shen, Journal of Materials Chemistry A, 2013, **1**, 2139-2143.
23. J. Zhao, F. Wang, P. Su, M. Li, J. Chen, Q. Yang and C. Li, Journal of Materials Chemistry, 2012, **22**, 13328-13333.
24. J. G. Kim, S. H. Lee, Y. Kim and W. B. Kim, ACS Applied Materials & Interfaces, 2013, **5**, 11321-11328.
25. S.-W. Kim, H.-W. Lee, P. Muralidharan, D.-H. Seo, W.-S. Yoon, D. K. Kim and K. Kang, Nano Research, 2011, **4**, 505-510.
26. G. Zhang, L. Yu, H. B. Wu, H. E. Hoster and X. W. D. Lou, Advanced Materials, 2012, **24**, 4609-4613.
27. L. Xiao, Y. Yang, J. Yin, Q. Li and L. Zhang, Journal of Power Sources, 2009, 194,1089-93.
28. Y. Li, B. Tan and Y. Wu, Nano Letters, 2008, **8**, 265-270.
29. P.-L. Taberna, S. Mitra, P. Poizot, P. Simon and J.-M. Tarascon, Nature Materials, 2006, **5**, 567-573.
30. C. K. Chan, H. Peng, G. Liu, K. McIlwrath, X. F. Zhang, R. A. Huggins and Y. Cui, Nature Nanotechnology, 2007, **3**, 31-35.
31. C. Sun, S. Rajasekhara, J. B. Goodenough and F. Zhou, Journal of the American Chemical Society, 2011, **133**, 2132-2135.
32. S. Ding, D. Zhang, J. S. Chen and X. W. D. Lou, Nanoscale, 2012, **4**, 95-98.
33. D. Larcher, G. Sudant, R. Patrice and J.-M. Tarascon, Chemistry of Materials, 2003, **15**, 3543-3551.

34. S.-W. Cao, Y.-J. Zhu, M.-Y. Ma, L. Li and L. Zhang, The Journal of Physical Chemistry C, 2008, **112**, 1851-1856.

35. L. Hu, H. Zhong, X. Zheng, Y. Huang, P. Zhang and Q. Chen, Scientific Reports, 2012, **2**, 986.

36. Y. Xiong, J. M. McLellan, J. Chen, Y. Yin, Z.-Y. Li and Y. Xia, Journal of the American Chemical Society, 2005, **127**, 17118-17127.

37. F. Fievet, J. Lagier and M. Figlarz, MRS Bulletin, 1989, **14**, 29-34.

38. M. Ocana, R. Rodriguez Clemente and C. J. Serna, Advanced Materials, 1995, **7**, 212-216.

39. V. K. LaMer and R. H. Dinegar, Journal of the American Chemical Society, 1950, **72**, 4847-4854.

40. F. Tao, C. Gao, Z. Wen, Q. Wang, J. Li and Z. Xu, Journal of Solid State Chemistry, 2009, **182**, 1055-1060.

41. R. Qiao, X. L. Zhang, R. Qiu, J. C. Kim and Y. S. Kang, Chemistry-A European Journal, 2009, **15**, 1886-1892.

42. L. Zhang, W. Wang, Z. Chen, L. Zhou, H. Xu and W. Zhu, Journal of Materials Chemistry, 2007, **17**, 2526-2532.

43. P. W. Voorhees, Journal of Statistical Physics, 1985, **38**, 231-252.

44. C. Yuan, L. Zhang, L. Hou, L. Zhou, G. Pang and L. Lian, Chemistry-A European Journal, 2014, **20**, 1-8.

45. H. Lv, L. Ma, P. Zeng, D. Ke and T. Peng, Journal of Materials Chemistry, 2010, **20**, 3665-3672.

46. C. Yuan, J. Li, L. Hou, L. Yang, L. Shen and X. Zhang, Journal of Materials Chemistry, 2012, **22**, 16084-16090.

47. G. Zhou, D.-W. Wang, F. Li, L. Zhang, N. Li, Z.-S. Wu, L. Wen, G. Q. Lu and H.-M. Cheng, Chemistry of Materials, 2010, **22**, 5306-5313.

48. H. Wang, L.-F. Cui, Y. Yang, H. Sanchez Casalongue, J. T. Robinson, Y. Liang, Y. Cui and H. Dai, Journal of the American Chemical Society, 2010, **132**, 13978-13980.

Hierarchical flowerlike $ZnMn_2O_4$ microspheres with high electrochemical performance as an anode material for Li-Ion batteries have been fabricated by a facile solvothermal method.